(Received 15 July 2025, Accepted 1 December 2026, Scheduled 26 February 2026)

Additive Manufacturing of a Luneburg Lens for Electromagnetic Applications

François Bordas, Adrien Belsola, and Pierre Sabouroux*

Aix Marseille Université, CNRS, Centrale Med, Institut Fresnel, Marseille, France

ABSTRACT: We present the design, fabrication, and experimental characterization of two 150 mm Luneburg lenses for X-band (10 GHz), produced by FFF (Fused Filament Fabrication) using standard PLA. The printed PLA permittivity was measured with a 7 mm coaxial cell and EpsiMu, yielding $\varepsilon_{r,\mathrm{PLA}} \approx 2.5$ at 100% infill; a volume-weighted mixing model with perimeter correction was used to set discrete radial infill fractions. Two infill patterns (grid and gyroid) were tested, and waveguide mounts were integrated for reproducible alignment. Insertion-loss tests give 1.5 dB (grid) and 1.1 dB (gyroid) at 10 GHz. Far-field measurements ($R = 1.5$ m) and Friis-based estimates yield peak gains of 20.5 dBi (grid) and 19.4 dBi (gyroid) (simulation: 20.8 dBi); the waveguide reference gain is 4.9 dBi. Near-field tests at $R = 0.15$ m show an on-axis S_{21} improvement of +2.33 dB, which corresponds to a low apparent near-field aperture efficiency (1.8–2.3%) while far-field efficiencies inferred from the measured gains are substantially higher (35–45%). These results confirm that discrete infill grading in low-cost FFF-printed PLA can realize effective Luneburg lenses at X-band, with quantifiable trade-offs among insertion loss, infill geometry, and realized aperture efficiency.

1. INTRODUCTION

With the growing demand for low-cost, efficient, and compact microwave components, the integration of advanced dielectric lenses into communication systems has become a prominent area of research [1, 3, 12, 14]. One notable example is the Luneburg lens, a spherical gradient-index lens capable of passively focusing incoming electromagnetic waves onto a single point, thereby enhancing antenna gain with minimal complexity and cost [1, 2, 4].

This focusing behavior is governed by a radial permittivity profile defined as:

$$\varepsilon(r) = 2 - \left(\frac{r}{R}\right)^2, \tag{1}$$

where r denotes the radial coordinate, and R is the lens radius. The resulting permittivity ranges from 2 at the center to 1 at the surface. As illustrated in Figure 1, this ideal continuous profile can be approximated by a discretized, additively manufactured Luneburg lens.

Recent advances in additive manufacturing have enabled the fabrication of gradient-index structures using cost-effective materials and single-extruder Fused Filament Fabrication (FFF) workflows [1–4, 6, 7, 12, 14]. Several strategies have been proposed to implement the required permittivity gradient, notably controlled infill density, engineered void patterns, and graded high-permittivity composites [3, 4, 6–9, 13, 14]. In our work, we employ such strategies within a low-cost FFF framework to realize Luneburg-type lenses; measured insertion losses at 10 GHz were approximately 1.1 dB for the gyroid segment and 1.5 dB for the grid segment. We also evaluated the lens in both far-field ($R = 1.5$ m) and near-field (guide-lens-guide at $R = 0.15$ m) configurations. Far-field measurements yield peak gains up to about 20.5 dBi (grid) and 19.4 dBi (gyroid), consistent with full-wave simulations and with aperture-based gain expressions used in antenna theory [1, 15]. Near-field measurements at 0.15 m show a clear on-axis S_{21} improvement of +2.33 dB when the lens is inserted; however, the conversion of this near-field gain into an effective aperture reveals a very small equivalent capture area (a few cm^2) compared to the physical lens area (176.7 cm^2), an apparent aperture efficiency of only a few percent. This distinction between near-field coupling gains and far-field aperture performance is important and has practical consequences for feed design and measurement strategy, an aspect that also appears in recent discussions of lens antennas and large-aperture systems [1].

The present study therefore sits at the intersection of several threads in the literature: reliable permittivity extraction and mixing-law design for FFF printed parts [5, 7, 10, 11, 14], practical 3D-printed lenses for transformation-optics and graded-index applications [1–4, 12, 14], the influence of infill geometry on mechanical and electromagnetic properties [6–9, 13], and the role of aperture efficiency and insertion loss in realistic devices [1, 15]. By combining material characterization, insertion-loss quantification, and both near- and far-field antenna measurements, we provide a complete experimental demonstration of low-cost Luneburg lenses manufactured by FFF and discuss the practical trade-offs for material selection, infill geometry, and feed engineering.

The remainder of this paper is organized as follows. Section 2 presents the electromagnetic characterization of the permittivity of Polylactic Acid (PLA), focusing on dielectric mea-

* Corresponding author: Pierre Sabouroux (pierre.sabouroux@fresnel.fr).

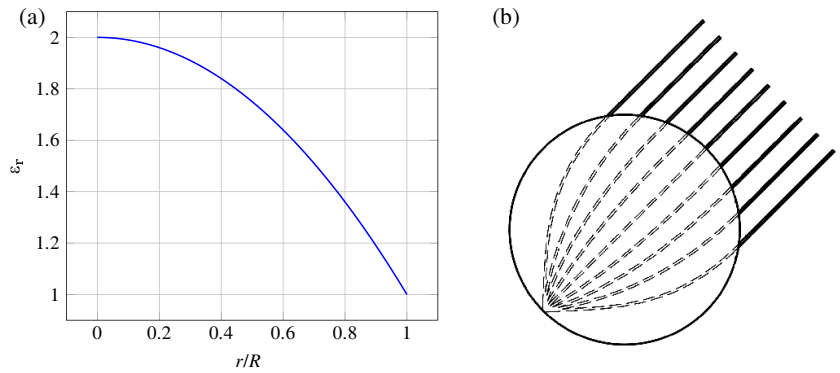

FIGURE 1. Comparison of the theoretical permittivity profile and a printed Luneburg lens. (a) Luneburg lens equation. (b) Luneburg lens visualization.

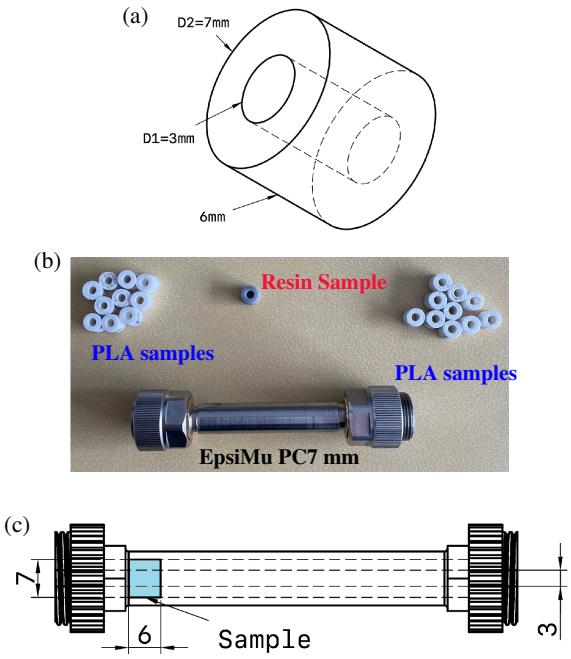

FIGURE 2. Sample preparation and measurement setup for permittivity extraction using the EpsiMu PC7 mm coaxial cell. (a) Geometry of the PLA samples (6 mm thickness). (b) PC7 mm coaxial cell without sample. (c) PC7 mm coaxial cell with sample (in blue) inserted.

surements. Section 3 details the geometric structure utilized for the Luneburg lens design. Section 4 outlines the measurement fundamentals and provides the governing equations. Section 5 describes the measurement of the Luneburg lenses, specifically looking at the far field to retrieve the lens gain. Section 6 is dedicated to the insertion loss characterization. Section 7 presents the near-field measurements of the Luneburg lens. Finally, Section 8 provides a discussion on the performance and limitations, while Section 9 concludes the paper

2. ELECTROMAGNETIC CHARACTERIZATION OF PLA

First, in order to implement the permittivity gradient effect through infill density variation during 3D printing, and to more generally enable the manufacturing of the Luneburg lens, it was necessary to experimentally determine the relative permittivity

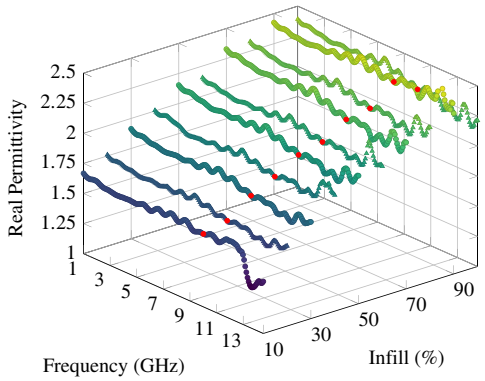

FIGURE 3. PLA real permittivity vs. frequency and infill density (0.4 mm nozzle). Red points: values at 10 GHz.

of Polylactic Acid (PLA). These measurements were performed at room temperature using the **EpsiMu** software in combination with a PC7 mm coaxial test cell, which features a 7 mm outer conductor diameter and a 3 mm inner conductor diameter.

Several PLA samples were prepared with infill densities ranging from 10% to 100%, using two different nozzle sizes: 0.2 mm and 0.4 mm. All samples were printed simultaneously to minimize variation due to temperature, material batch, or humidity. Each printed sample had a thickness of 6 mm, as illustrated in Figure 2(a).

In addition, a single resin sample with 100% infill was tested. Figure 2(b) shows the coaxial cell, and Figure 2(c) illustrates the PC7 mm cell with a sample inserted for measurement.

Figure 3 and Figure 4 show the real part of the permittivity and the imaginary part of the samples printed using a 0.4 mm nozzle diameter.

Our application target is a lens operating at 10 GHz. Figure 5 reproduces the measured permittivity at 10 GHz as a function of infill density for two different nozzle diameters (0.4 mm and 0.2 mm). The blue and orange marker series correspond to the 0.4 mm and 0.2 mm nozzles, respectively; the dashed lines are linear fits used to highlight the trend.

Figure 5 shows a non-zero intercept at 0% infill for both curves: an intrinsic permittivity is present even when the nominal infill is zero. This effect arises from the solid walls required by the FFF printing process to contain the infill. These walls contain residual material and therefore contribute a non-negligible volume fraction of the sample, producing an appar-

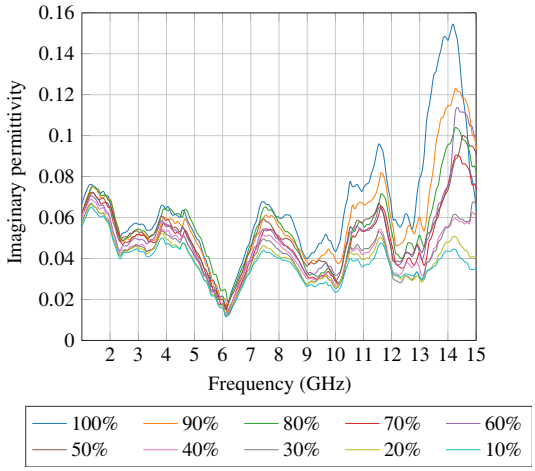

FIGURE 4. PLA imaginary permittivity vs. frequency and infill density (0.4 mm nozzle).

ent baseline permittivity that must be accounted for when interpreting low-infill measurements.

The influence of the walls can be estimated using a volume-based mixing approach. For a cylindrical sample, the wall volumes can be approximated as:

$$V_{\text{top\&bot}} = 2\pi L_{\text{th}}(r_2^2 - r_1^2), \quad (2)$$

$$V_{\text{outerWall}} = \pi(h - 2L_{\text{th}})\left(r_2^2 - (r_2 - w_{\text{th}})^2\right), \quad (3)$$

$$V_{\text{innerWall}} = \pi(h - 2L_{\text{th}})\left((r_1 + w_{\text{th}})^2 - r_1^2\right), \quad (4)$$

$$V_{\text{totalWall}} = V_{\text{outerWall}} + V_{\text{innerWall}} + V_{\text{top\&bot}}. \quad (5)$$

In these expressions:

- $h = 6$ is the sample thickness;
- w_{th} is the printed wall thickness (typical slicing defaults give $w_{\text{th}} = 0.42$ for a 0.4 nozzle and $w_{\text{th}} = 0.22$ for a 0.2 nozzle),
- $r_1 = D_1/2$ and $r_2 = D_2/2$ are the inner and outer radii of the printed cylinder;
- L_{th} is the layer height (we use $L_{\text{th}} = 0.2$).

Based on the measured permittivity at 10 GHz for fully dense (100%) samples and in Eqs. (2)–(5), we compute a theoretical curve that quantifies the contribution of the printed walls to the intrinsic permittivity of the specimens. The model assumes a simple volume-weighted mixing law, where the nominal infill fraction is denoted by α (with $0 \leq \alpha \leq 1$), and air is approximated by $\varepsilon_{\text{air}} \approx 1$.

The effective permittivity of the measured sample is then written as

$$\varepsilon_r = f_1\varepsilon_{\text{PLA}} + (1 - f_1)\Big(\alpha\varepsilon_{\text{PLA}} + (1 - \alpha)\varepsilon_{\text{air}}\Big),$$

where

- $f_1 = V_{\text{totalWall}}/V_{\text{sample}}$ is the wall volume fraction defined above;

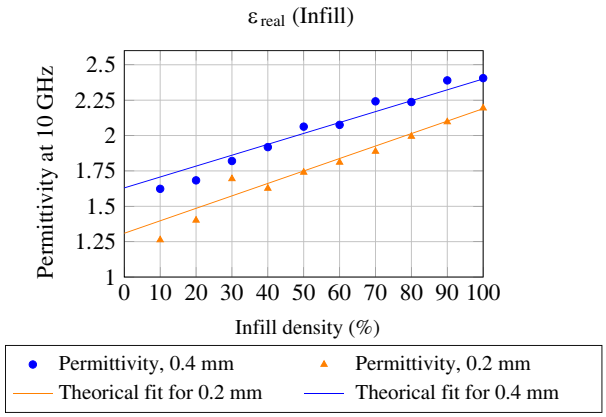

FIGURE 5. Comparison of real permittivity at 10 GHz for two nozzle diameters.

- ε_{PLA} is the bulk PLA permittivity (taken here from the measured 100% infill sample for each nozzle diameter); and
- α is the nominal infill expressed as a decimal (e.g., $50\% \Rightarrow \alpha = 0.5$).

With $\varepsilon_{\text{air}} \approx 1$, the expression is simplified to

$$\varepsilon_r = f_1\varepsilon_{\text{PLA}} + (1 - f_1)\left(\alpha\varepsilon_{\text{PLA}} + 1 - \alpha\right).$$

In practice, we use the measured ε_{PLA} (100% curve) for each nozzle diameter and compute ε_r as a function of α. The resulting theoretical curves are plotted in Figure 5 (labeled "Theoretical fit", shown in the orange and blue lines) and match the experimental marker data. This wall-volume correction demonstrates why the measured permittivity does not drop to air at nominal 0% infill and provides a straightforward geometric correction for lens design at 10 GHz.

Based on the results presented in Figures 3, 4, and 5, the real part of the relative permittivity exhibits a clearly linear behavior with respect to infill density. Figure 5 further demonstrates that this relationship is influenced by the nozzle diameter, due to the intrinsic permittivity contribution of the sample walls. These walls, although essential for ensuring the mechanical integrity of the lens and avoiding direct exposure of the infill structure, introduce an additional permittivity component that must be considered. Therefore, this wall-induced effect must be taken into account in the electromagnetic design of the Luneburg lens to ensure an accurate control of the spatial permittivity distribution. In the context of our application, the imaginary part of the permittivity is considered negligible, and only the real part is used in the electromagnetic modeling and design process.

3. GEOMETRIC STRUCTURE USED FOR LUNEBURG LENS DESIGN

Based on the electromagnetic characterization of PLA, the effective relative permittivity of a printed specimen can be approximated by a linear volume-weighted mixing rule (see [2]):

$$\varepsilon_{\text{target}} = \varepsilon_1 F_1 + \varepsilon_2 F_2, \quad (6)$$

where ε_1 is the relative permittivity of PLA at 100 infill, ε_2 is the relative permittivity of air (approximately 1), and F_1 and $F_2 = 1 - F_1$ are the volume fractions of PLA and air, respectively. This model provides a practical way to predict the effective permittivity as a function of nominal infill density — a necessary capability to control the radial permittivity gradient required for Luneburg-lens design.

3.1. Radial Permittivity Gradient Strategy

The design objective is a radial permittivity profile varying from $\varepsilon_r = 2.0$ at the centre to $\varepsilon_r = 1.0$ at the outer surface. We implement this profile by setting different nominal infill fractions in concentric shells during FFF 3D printing. Using the linear mixing assumption and writing air permittivity as unity, the nominal PLA volume fraction required to obtain a target permittivity $\varepsilon_{\text{target}}$ is

$$F_1 = \frac{\varepsilon_{\text{target}} - 1}{\varepsilon_{\text{PLA}} - 1}, \tag{7}$$

where ε_{PLA} is the experimentally measured permittivity of the fully dense PLA sample, and F_1 is the nominal infill ratio to be set in the slicer (expressed as a fraction between 0 and 1, or as a percentage).

However, printed parts include solid perimeters (walls) that occupy a non-negligible volume fraction, even when the interior infill fraction is low or nominally zero. These walls produce an intrinsic baseline permittivity: neglecting them leads to overestimating how close the measured permittivity gets to air at low infill, thus biasing lens performance predictions.

To illustrate the layered implementation we use in the lens, Figure 6 shows the concentric-shell discretization and its corresponding target permittivity values.

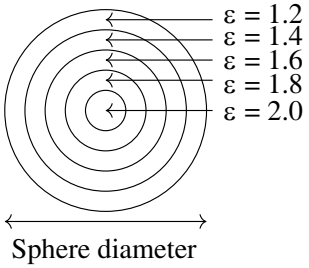

FIGURE 6. Layered implementation: concentric shells and their target permittivity values.

To mitigate the wall contribution, we compute the wall and shell volumes. For the external spherical shell (outermost layer), we use:

$$V_{\text{shell}} = \frac{4}{3}\pi \left(r_5^3 - r_4^3\right), \tag{8}$$

$$V_{\text{wall,ext}} = \frac{4}{3}\pi \left(r_5^3 - (r_5 - w_{\text{th}})^3\right), \tag{9}$$

with r_5 being the outer radius of the external shell (layer 5), r_4 the radius of the previous shell, and w_{th} the printed wall (perimeter) thickness. Typical slicing defaults used here are $w_{\text{th}} = 0.44$ for a 0.4 mm nozzle and $w_{\text{th}} = 0.22$ for a 0.2 mm nozzle.

The wall fraction of the external shell is

$$f_{\text{wall,ext}} = \frac{V_{\text{wall,ext}}}{V_{\text{shell}}} = \frac{r_5^3 - (r_5 - w_{\text{th}})^3}{r_5^3 - r_4^3}. \tag{10}$$

For illustration, assuming five concentric shells of equal radial thickness in a lens of total diameter 150 mm (so $r_5 = 75$ and $r_4 = 60$), and using $w_{\text{th}} = 0.44$, we obtain $f_{\text{wall,ext}} \approx 3.6\%$. Although small, this contribution must be taken into account for precise permittivity control.

The computed infill percentages for the five concentric layers (derived via Eq. (7) with $\varepsilon_{\text{PLA}} = 2.5$) are summarized in Table 1.

TABLE 1. Required infill percentages for a 5-layer spherical lens (total diameter 150 mm, $\varepsilon_{\text{PLA}} = 2.5$).

Layer	$\varepsilon_{\text{target}}$	Infill F_1 (%)
5	1.2	10
4	1.4	27
3	1.6	40
2	1.8	53
1	2.0	66

3.1.1. Infill Pattern: Grid vs. Gyroid

Beyond the infill fraction itself, the choice of infill *pattern* affects mechanical strength and may slightly influence electromagnetic properties (phase delay, effective anisotropy). Two patterns were evaluated: the *grid* pattern (faster, lower stiffness) and the *gyroid* pattern (slower, better isotropy and strength). Figure 7 shows cross-sectional views of the printed lens central plane, illustrating the two patterns and the associated infill distribution.

3.2. Practical Mounting and Flange Design

To simplify the alignment and attachment of the X-band rectangular waveguide during measurement and use, a dedicated guide flange (bracket) was integrated on the lens surface. This flange allows quick mechanical alignment and reproducible positioning of the waveguide onto the lens; metallic inserts secure a rigid, centred connection that avoids air gaps and mechanical play.

Figure 8 shows the manufactured lenses and the mounting system used in the measurements.

3.2.1. Selective Wall Removal at Waveguide Interface (Figure 8)

To reduce the perturbing influence of the printed wall at the waveguide aperture, we selectively removed the perimeter at the guide exit while preserving the rest of the sphere walls. This local modification lowers the intrinsic permittivity contribution directly in the coupling region without compromising the global mechanical integrity.

Figure 8 illustrates: (a) the flange and alignment system, (b) the assembled lens with mounting, and (c) a close-up of the

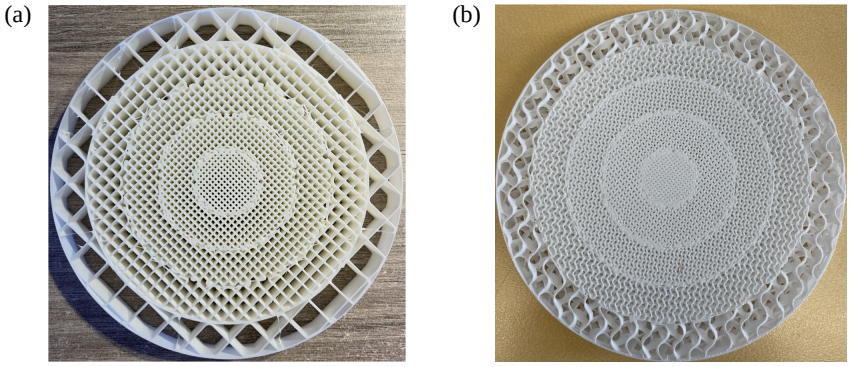

FIGURE 7. Cross-sectional views of the printed spherical lenses showing the infill patterns used for each concentric shell. (a) Grid pattern. (b) Gyroid pattern.

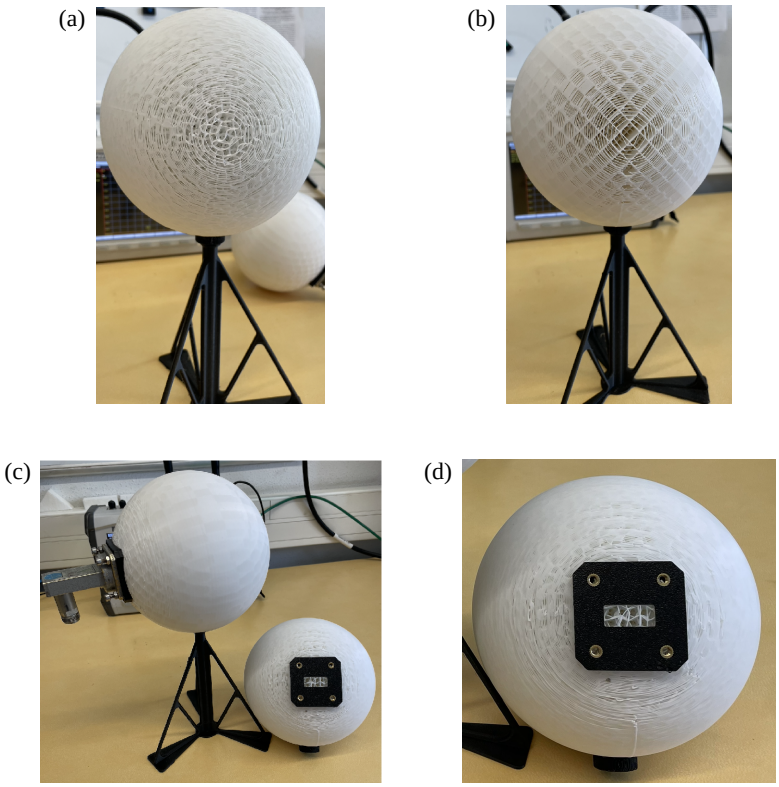

FIGURE 8. Manufactured lenses with practical mounting enhancements and different infill patterns. (a) Lens with gyroid infill. (b) Lens with grid infill. (c) Waveguide mounting system and tripod. (d) Zoom on waveguide interface detail.

waveguide exit showing the removed wall (schematic/photo). Replace the placeholders below with the final images one prefers for panels (a)–(c).

3.3. Manufacturing Note: Single-Perimeter Effects

Printing the outermost shell with a single perimeter (one exterior pass of thickness w_{th}) may produce visible surface irregularities and local thickness inconsistency. Although a single perimeter helps reduce the wall volume contribution to permittivity, it introduces an undesirable variation of the external surface quality and local dielectric thickness. In our production tests, we therefore balanced the following trade-offs:

- **Minimise wall-induced permittivity bias** by reducing unnecessary perimeters at the waveguide interface (selective removal), and
- **Preserve mechanical robustness** by keeping perimeters elsewhere or increasing nominal infill for layers where mechanical support is critical.

The discrete permittivity gradient implemented in the physical lens and the computed infill percentages for the five concentric layers are summarized in Table 1. Figures 6–8 show

the layered implementation, evaluated infill patterns, manufactured lenses, and mounting/flange details, respectively.

4. MEASUREMENT FUNDAMENTALS

All measurements were performed with an Anritsu MS2038C VNA at 10 GHz (free-space wavelength $\lambda = 0.03$ m). The relations used to interpret transmission data are the Friis equation

$$\frac{P_r}{P_t} = G_t G_r \left(\frac{\lambda}{4\pi R}\right)^2 \tag{11}$$

and the aperture-based gain expression

$$G_{\text{dBi}} = 10\log_{10}\left(\frac{4\pi\Sigma}{\lambda^2}\right), \quad \Sigma = S f_g, \tag{12}$$

where S is the physical aperture, and f_g is an efficiency factor. The far-field distance is $R_{\text{far}} = 2D^2/\lambda$.

With the apertures used here, the theoretical gains at 10 GHz are:

- Rectangular X-band waveguide, 2.25×1.00 cm: $G_{\text{theor}} \approx 4.97$ dBi.
- Horn antenna, 7.5×5.0 cm: $G_{\text{theor}} \approx 17.19$ dBi.
- Circular Luneburg lens, $D = 150$ mm ($r = 75$ mm): $G \approx \frac{4\pi^2 r^2}{\lambda^2} \approx 246 \Rightarrow G_{\text{theor}} \approx 23.92$ dBi.

Far-field distances at 10 GHz (for reference): lens ($D = 0.15$ m) $R_{\text{far}} \approx 1.50$ m; horn ($D = 0.075$ m) $R_{\text{far}} \approx 0.38$ m.

These compact relations (Eqs. (11)–(12)) are referenced in the measurement section that follows.

5. MEASUREMENT OF THE LUNEBURG LENSES

Measurements were carried out for both lens variants (grid and gyroid infill). All transmission configurations were measured with a separation of $R = 1.5$ m between the phase centers. This measurement distance satisfies the far-field condition for the 150 mm lens and exceeds the horn far-field distance.

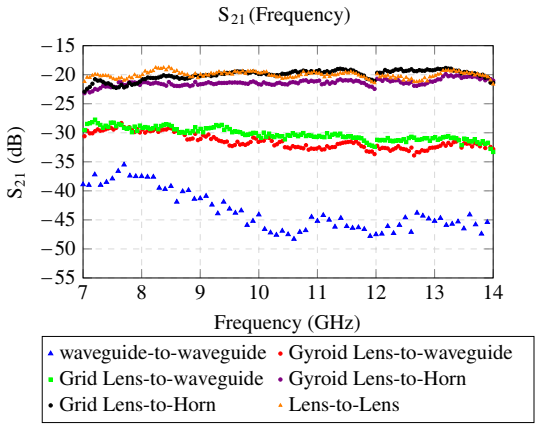

FIGURE 9. Measured transmission coefficients (S_{21}) for the four tested configurations: waveguide-to-waveguide, lensto-waveguide, lens-to-lens, and lens-to-horn antenna.

Measured transmission coefficients are shown in Figure 9. From the waveguide-to-waveguide transmission at $R = 1.5$ m and applying Eq. (11), the measured waveguide gain is

$$G_{\text{guide,meas}} \approx 4.9 \text{ dBi}.$$

Using this measured reference, the lens gains retrieved from the lens-to-waveguide transmissions are:

- Gyroid lens: $G_{\text{lens,gyroid}} \approx 19.4$ dBi.
- Grid lens: $G_{\text{lens,grid}} \approx 20.5$ dBi.

From the lens-to-horn transmission configurations, the horn gain is back-calculated, yielding

$$G_{\text{horn}} \approx 15.58 \text{ dBi (from grid lens)},$$
$$G_{\text{horn}} \approx 14.86 \text{ dBi (from gyroid lens)}.$$

For comparison with measurements, electromagnetic simulations were performed in Computer Simulation Technology (CST). The simulated peak E-plane gain is 20.8 dBi (see Figure 10), consistent with the measured lens gains above.

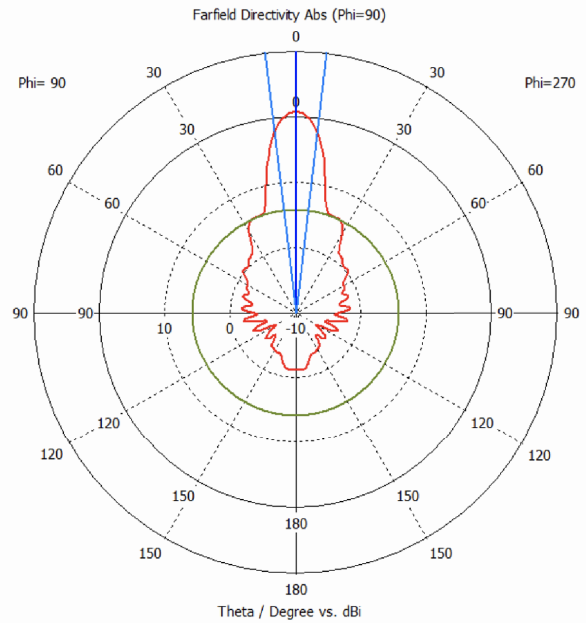

FIGURE 10. Simulated radiation pattern in the E-plane at 10 GHz, showing a peak gain of 20.8 dBi.

6. INSERTION LOSS CHARACTERIZATION

To quantify the insertion losses introduced by the 3D-printed Luneburg lens materials, a simple and reproducible waveguide-based measurement was carried out. A representative segment of each lens (grid and gyroid infill) was inserted directly inside a standard rectangular waveguide section, as illustrated in Figure 11. The method allows a direct comparison of transmission through the printed dielectric structures under controlled and well-defined boundary lens piece precisely machined to fit the waveguide aperture. All measurements were performed at 10 GHz using an Anritsu MS2038C vector network analyzer. Prior to testing, a full two-port conditions. Two 100 mm waveguide extensions were assembled to accommodate the device

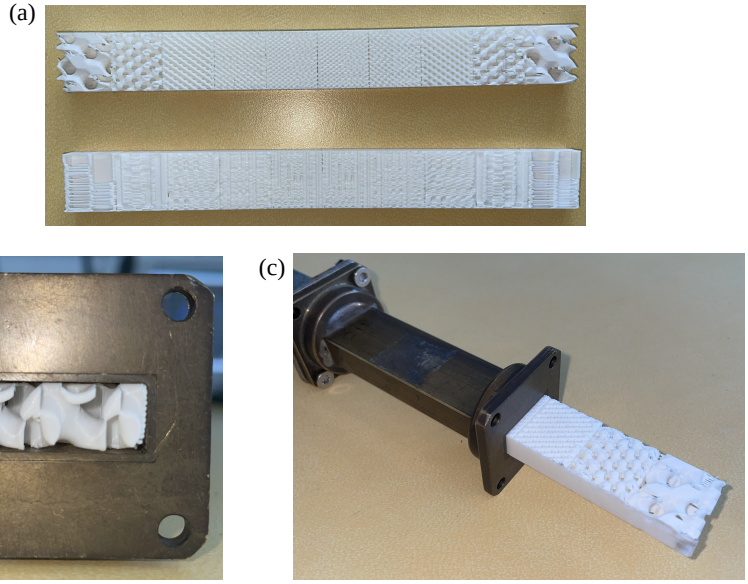

FIGURE 11. Photographs of the insertion-loss test pieces and their placement inside the rectangular waveguide. (a) Grid and gyroid pieces used as DUTs. (b) Gyroid piece inserted into the rectangular waveguide. (c) Gyroid piece partially inserted into the rectangular waveguide.

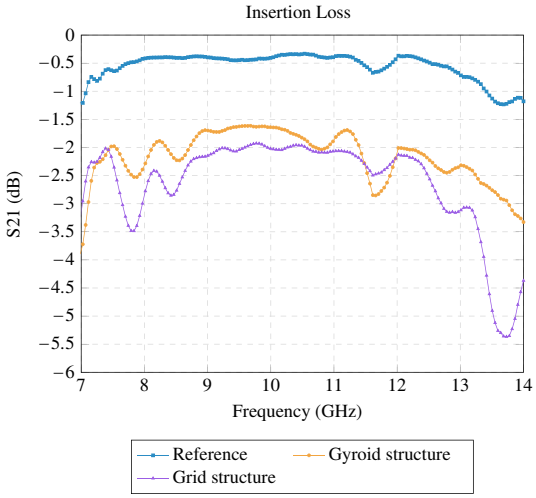

FIGURE 12. Measured insertion loss as a function of frequency. The reference corresponds to the empty waveguide (air, no DUT).

under test (DUT), each consisting of a short lens piece precisely machined to fit the waveguide aperture. All measurements were performed at 10 GHz using an Anritsu MS2038C vector net work analyzer. Prior to testing, a full two-port short-open-load-through (SOLT) calibration was performed using a coax-to-coax through connection, without the waveguide sections, in order to quantify the baseline losses of the empty measurement system.

The measured transmission data are presented in Figure 12. Three measurement traces are shown: the empty-waveguide reference (extension only, blue trace), the waveguide containing the gyroid-filled lens segment (orange trace), and the waveguide containing the grid-filled lens segment (purple trace). Insertion loss for each DUT is obtained by comparing the DUT trace to the empty-waveguide reference at the measurement frequency (10 GHz).

From the data in Figure 12, the insertion losses at 10 GHz are:

- Grid infill: ≈ 1.5 dB,
- Gyroid infill: ≈ 1.1 dB.

These values are reported without further correction and correspond to the short-piece insertion configuration described above. The observed difference between grid and gyroid fillings may arise from different effective permittivities and internal scattering within the printed structures; a more detailed analysis (thickness dependence, repeatability, and environmental sensitivity) is left for subsequent work.

7. NEAR-FIELD MEASUREMENT OF THE LUNEBURG LENS

Measurements were performed at $f = 10$ GHz with WR-90 waveguides. The on-axis transmission coefficients measured at a separation of $R = 0.15$ m (distance between waveguide faces (see Fig. 13)) are

$$S_{21,\text{empty}} = -25.45\,\text{dB}, \quad S_{21,\text{lens}} = -23.12\,\text{dB},$$

i.e., an on-axis transmission improvement of $\Delta S_{21} = +2.33$ dB when the 3D-printed Luneburg lens is inserted (see Fig. 14).

The free-space path loss at $R = 0.15$ m and $\lambda = 0.03$ m (10 GHz) is

$$\text{FSPL} = 20\log_{10}\left(\frac{4\pi R}{\lambda}\right) \approx 35.96\,\text{dB}.$$

From the empty guide-guide measurement and Friis in dB,

$$S_{21} = G_t + G_r - \text{FSPL},$$

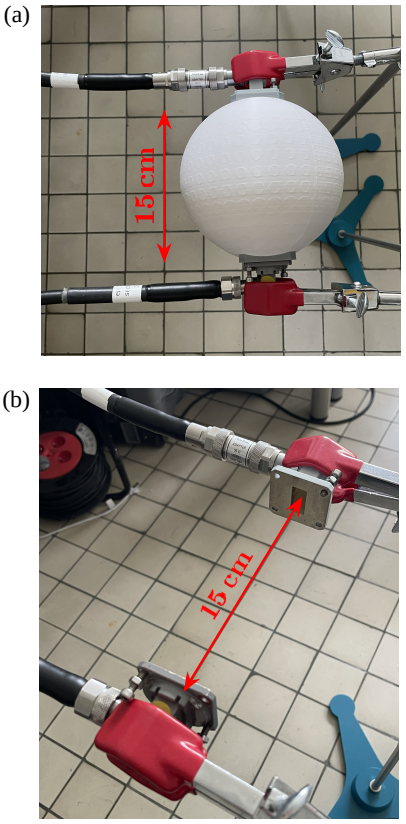

FIGURE 13. Photographs of the experimental setups used for the transmission measurements, with 15 cm distance indicated. (a) Guide-lens-guide configuration (top view). (b) Guide-guide reference configuration (no lens).

and assuming identical guide apertures on both sides, the equivalent guide gain is

$$G_{\text{guide}} \approx \frac{S_{21,\text{empty}} + \text{FSPL}}{2} = \frac{-25.45 + 35.96}{2} \approx 5.26\,\text{dBi}.$$

The measured change in transmission when the lens is inserted is

$$\Delta S_{21} = S_{21,\text{lens}} - S_{21,\text{empty}} = +2.33\,\text{dB}.$$

The antenna gain of an aperture can be written as

$$G = \frac{4\pi A_e}{\lambda^2},$$

where A_e is the effective aperture. This expression can be inverted to obtain

$$A_e = \frac{G\lambda^2}{4\pi}, \quad \eta_A = \frac{A_e}{A_g},$$

with A_g being the geometric capture area of the antenna (here the physical aperture area).

For the guide we use $A_{g,\text{guide}} = 2.25\ \text{cm}^2$ (value used for the reference). Converting $G_{\text{guide}} = 5.26$ dBi to linear scale and applying the formula with $\lambda = 3$ cm yields

$$A_{e,\text{guide}} \approx 2.40\ \text{cm}^2.$$

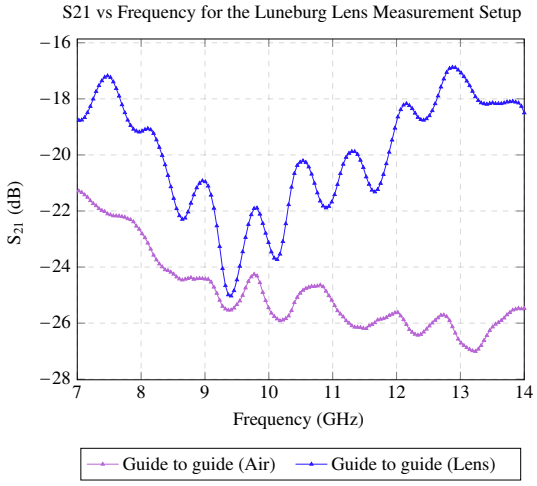

FIGURE 14. Measured transmission coefficient $|S_{21}|$ for guide-guide without lens and with the Luneburg lens inserted at $R = 0.15$ m.

Thus, the apparent aperture efficiency of the guide is

$$\eta_{A,\text{guide}} \approx \frac{2.40}{2.25} \approx 1.06,$$

i.e., about 106% (this value above unity indicates a small measurement uncertainty on the reference, on the order of 6%).

If the lens is interpreted as replacing one aperture (lens-to-guide configuration), the apparent on-axis gain of the lens-fed aperture is

$$G_{\text{lens,apparent}} = S_{21,\text{lens}} + \text{FSPL} - G_{\text{guide}} \approx 7.59\,\text{dBi}.$$

Using this gain,

$$A_{e,\text{lens}} \approx 4.11\,\text{cm}^2,$$

and with the lens geometric area

$$A_{g,\text{lens}} = \pi(7.5\,\text{cm})^2 \approx 176.7\,\text{cm}^2,$$

the aperture efficiency is

$$\eta_{A,\text{lens}} \approx \frac{4.11}{176.7} \approx 0.023(2.3\%).$$

If we account for a similar relative uncertainty as observed on the guide (6%), the efficiency range becomes approximately [0.0219; 0.0247] (i.e., about 2.2–2.5%).

If instead the lens affects both feed apertures symmetrically, the measured $\Delta S_{21} = 2.33$ dB corresponds to about 1.17 dB gain increase per aperture. In that symmetric interpretation, the per-aperture on-axis gain with the lens is

$$G_{\text{per face,with lens}} \approx G_{\text{guide}} + 1.17 \approx 6.42\,\text{dBi},$$

which gives

$$A_{e,\text{lens,sym}} \approx 3.14\,\text{cm}^2, \quad \eta_{A,\text{lens,sym}} \approx \frac{3.14}{176.7} \approx 0.0178.$$

Despite the near-field measurement geometry, the insertion of the 3D-printed Luneburg lens produces a clear and measurable increase in S_{21} (+2.33 dB at 10 GHz). However, when these measured gains are converted back to equivalent capture

area, the effective reception area is very small compared to the physical lens area: on the order of a few cm^2 versus $176.7\,\mathrm{cm}^2$ geometric area, i.e., an apparent aperture efficiency of roughly 1.8–2.3% at the 15 cm measurement distance. This indicates that, in the present feed and distance configuration, the large lens aperture is strongly under-illuminated, and much of the geometric area does not contribute effectively to received power. The above numerical values have been checked and are consistent with the measured S_{21} values and the FSPL used.

8. DISCUSSION

The experimental results demonstrate that 3D-printed Luneburg lenses substantially improve the transmission between a standard WR-90 waveguide and several receiving configurations. Using the measured transmission data, the waveguide reference gain was found to be approximately $4.9\,\mathrm{dBi}$. From the lens-to-waveguide measurements, we retrieved peak gains of $19.4\,\mathrm{dBi}$ for the gyroid lens and $20.5\,\mathrm{dBi}$ for the grid lens. Electromagnetic simulations (peak E-plane gain $20.8\,\mathrm{dBi}$) are consistent with these measured values.

Insertion loss measurements were performed by placing short printed segments inside a rectangular waveguide and comparing the transmitted power to an empty-waveguide reference. At 10 GHz, the measured insertion losses are approximately $1.1\,\mathrm{dB}$ for the gyroid segment and $1.5\,\mathrm{dB}$ for the grid segment. These insertion losses quantify the material and structural losses introduced by the printed dielectric and must be considered when comparing measured antenna gains to the ideal aperture theory.

The measured lens gains translate to substantial aperture efficiencies compared to the lens geometric area. Using

$$A_e = \frac{G\lambda^2}{4\pi}, \quad \eta_A = \frac{A_e}{A_g},$$

with $A_g = \pi(D/2)^2$ and $D = 0.15\,\mathrm{m}$, the measured gains give the following effective apertures and efficiencies: for $G = 19.4\,\mathrm{dBi}$ (gyroid) $\eta_A \approx 35\%$, and for $G = 20.5\,\mathrm{dBi}$ (grid) $\eta_A \approx 45\%$. These efficiencies indicate that the printed lenses capture a large fraction of their physical aperture in the far-field measurement configuration ($R = 1.5\,\mathrm{m}$), despite the discrete, piecewise implementation of the permittivity gradient and measured insertion losses.

It is useful to contrast the above far-field results with the near-field measurements made at 0.15 m (guide-lens-guide). In that near-field geometry, the lens insertion produced an on-axis S_{21} improvement of $+2.33\,\mathrm{dB}$. Interpreting this near-field result as an apparent per-aperture gain leads to much lower apparent efficiencies (order of a few percent, 1.8–2.3%) because the feed under-illuminates the large lens aperture, and the measurement is carried out inside the lens Fraunhofer distance. Thus, near-field S_{21} improvements are useful for quantifying local coupling gains and evaluating feed-lens matching, but they do not substitute far-field gain and efficiency measurements.

Possible origins of the observed differences between the two printed designs are as follows:

- small variations in effective permittivity distribution caused by differences in infill geometry and local volume fraction;
- slight differences in printed geometry (dimensional tolerances, surface roughness) and in the selective perimeter removal at the waveguide interface;
- different internal scattering behaviour: gyroid and grid patterns produce different sub-wavelength structure geometries that affect phase uniformity and internal scattering losses;
- the measured insertion losses (1.1–1.5 dB), which reduce the realized gain and may differ slightly between infill types.

From a manufacturing and practical viewpoint, the two infill patterns present trade-offs:

- the grid infill is faster to print and therefore attractive when rapid prototyping or short production time is required; it delivered the highest measured gain in this study (20.5 dBi);
- the gyroid infill provides more isotropic mechanical behaviour and generally better resistance to deformation, which is advantageous for robust, load-bearing or vibration-prone applications; it showed slightly lower insertion loss and a marginally lower gain (19.4 dBi), which may reflect its different dielectric microstructure.

These mechanical differences suggest that the choice of infill should be guided both by electromagnetic performance and by mechanical/production constraints.

Material considerations and future work. The present results, obtained with standard PLA (and limited resin tests), show that low-cost FFF approaches can yield high-performance dielectric lenses. To further improve performance and better separate material loss from geometric/illumination effects, a systematic material study is recommended. Candidate filament and resin materials to characterize (permittivity and loss tangent) include Polyethylene Terephthalate Glycol (PETG), Acrylonitrile Styrene Acrylate (ASA), Acrylonitrile Butadiene Styrene (ABS), and Thermoplastic Polyurethane (TPU), as well as low-loss printable resins. For each material, it is important to measure both the real part of the permittivity and the loss tangent at the operating frequency (e.g., using the EpsiMu PC7 mm cell or similar), and to repeat insertion-loss tests on representative printed structures. These data will enable:

- selection of low-loss materials that reduce insertion loss and increase realized gain;
- optimization of infill fraction and pattern for a given material to reach the target permittivity profile with minimal dissipation;
- trade-off analyses between mechanical robustness (gyroid advantage) and printing time/cost (grid advantage).

We note that resin should be treated as one material family among several to test; the discussion here focuses on a range of FFF filaments because they are widely available and convenient for large lumps, but comparative testing of resins (including low-loss formulations) remains valuable.

Recommendations for further characterization and validation. To complete the electromagnetic assessment and to support quantitative comparisons, we recommend:

1. direct dielectric characterization (real and imaginary parts) of PETG, ASA, ABS, and TPU filaments printed with the same process settings used for lenses;
2. measurement of S_{11} (reflection) on the mounted waveguide-lens interface to quantify mismatch losses and to separate mismatch from material absorption;
3. far-field pattern measurements ($R \gtrsim 1.5\,\mathrm{m}$) or NF (Near Field) $\rightarrow$ FF (Far Field) ransformations from planar/scan probes to obtain full 2D radiation patterns and accurate directivity values;
4. parameter sweeps of feed position and orientation to optimize the feed-to-lens coupling and minimize under-illumination or phase errors;
5. a thickness-dependence study for insertion loss (different segment lengths) to separate surface/interface effects from bulk material losses and scattering.

In summary, the measured gains (19.4 and 20.5 dBi), moderate insertion losses (1.1–1.5 dB), and agreement with simulation (20.8 dBi) together indicate that discrete, 3D-printed permittivity gradients can effectively approximate a Luneburg lens at X-band. The printed lenses combine good electromagnetic performance with low fabrication cost and short print times, and they offer a flexible platform for further optimization through material selection, infill geometry tuning, and improved feed engineering.

9. CONCLUSION

This work demonstrates the feasibility and competitive performance of low-cost, 3D-printed Luneburg lenses realized by discrete permittivity gradients. Experimental measurements confirm that these lenses substantially improve transmission gain compared to a bare waveguide and compare favourably with a standard horn antenna. The grid lens reached a measured peak gain of 20.5 dBi and the gyroid lens 19.4 dBi; these values closely match the simulated peak gain of 20.8 dBi.

Measured insertion losses of representative printed segments were moderate, approximately 1.5 dB for the grid pattern and 1.1 dB for the gyroid pattern at 10 GHz. These insertion losses partly explain the difference between the ideal aperture theory and the realized gain and must be accounted for when the overall system performance is assessed.

From the measured far-field gains and lens geometric area ($D = 150\,\mathrm{mm}$), we obtain effective apertures and aperture efficiencies of the order of tens of percent: the gyroid lens corresponds to an aperture efficiency of approximately 35%, while the grid lens reaches about 45%. These efficiencies show that the discrete, infill-based approximation of the Luneburg gradient captures a large fraction of the lens physical aperture in the far-field measurement configuration. By contrast, near-field measurements at 0.15 m (guide-lens-guide) yield a local, apparent per-aperture gain in the range 6.4–7.6 dBi and a much lower apparent aperture efficiency (roughly 1.8–22.3%), reflecting under-illumination and near-field coupling; such near-field figures should therefore be interpreted as local coupling indicators rather than far-field performance metrics.

The comparison between the two infill designs highlights relevant trade-offs. The grid infill is faster to print and produces the highest measured gain in this study, while the gyroid infill provides more isotropic mechanical properties and slightly lower insertion loss. These mechanical differences (gyroid = more isotropic, grid = faster printing) should guide design choices depending on whether electromagnetic performance, mechanical robustness, or manufacturing throughput is prioritized.

For further performance improvements and a more complete understanding of loss mechanisms, systematic material characterization is required. We recommend dielectric measurements (real permittivity and loss tangent at X-band) and insertion-loss tests for candidate printing materials, such as PETG, ASA, ABS, and TPU, in addition to the already tested PLA and resins. These data will allow the selection of lower-loss materials, optimization of infill fraction and pattern to achieve target permittivity with minimal dissipation, and informed trade-offs between mechanical strength and electromagnetic performance.

Finally, to fully validate and compare lens designs, we advise the following characterization steps in future work: (i) full far-field pattern measurements (or NF $\rightarrow$ FF transformations) to obtain complete directivity and sidelobe information; (ii) S_{11} measurements on the mounted waveguide-lens interface to quantify mismatch losses; (iii) feed-position sweeps to optimize illumination and minimize phase errors; and (iv) parametric studies of infill geometry and printed wall thickness to separate geometric scattering from bulk material losses.

In summary, discrete, 3D-printed Luneburg lenses produced by standard FFF processes combine good electromagnetic performance, moderate insertion loss, and very low fabrication cost, offering a flexible platform for rapid prototyping and for further optimization through material selection and infill design.

REFERENCES

[1] Munina, I., I. Grigoriev, G. O'donnell, and D. Trimble, "A review of 3D printed gradient refractive index lens antennas," *IEEE Access*, Vol. 11, 8790–8809, 2023.

[2] Grigoriev, I., I. Munina, and D. Zelenchuk, "3D printed Ku band cylindrical luneburg lens," in *Journal of Physics: Conference Series*, Vol. 2015, No. 1, 012095, 2021.

[3] Zhang, S., R. K. Arya, S. Pandey, Y. Vardaxoglou, W. Whittow, and R. Mittra, "3D-printed planar graded index lenses," *IET Microwaves, Antennas & Propagation*, Vol. 10, No. 13, 1411–1419, Oct. 2016.

[4] Pourahmadazar, J., B. S. Virdee, and T. A. Denidni, "Advancing into millimeter wavelengths for IoT: Multibeam modified planar

luneburg lens antenna with porous plastic material," *Electronics*, Vol. 13, No. 9, 1605, Apr. 2024.

[5] Baker-Jarvis, J. R., M. D. Janezic, J. H. Grosvenor, Jr., and R. G. Geyer, "Transmission/refection and short-circuit line methods for measuring permittivity and permeability," NIST Technical Note 1355 (TN 1355), National Institute of Standards and Technology (NIST), Boulder, CO, USA, May 1992.

[6] Colella, R., F. P. Chietera, and L. Catarinucci, "Analysis of FDM and DLP 3D-printing technologies to prototype electromagnetic devices for RFID applications," *Sensors*, Vol. 21, No. 3, 897, Jan. 2021.

[7] Hu, H., S. Sinha, N. Meisel, and S. G. Bilén, "Permittivity of 3D-printed nylon substrates with different infill patterns and densities for design of microwave components," *Designs*, Vol. 4, No. 3, 39, Sep. 2020.

[8] Maharjan, G. K., S. Z. Khan, S. H. Riza, and S. H. Masood, "Compressive behaviour of 3D printed polymeric gyroid cellular lattice structure," in *IOP Conference Series: Materials Science and Engineering*, Vol. 455, 012047, Telangana, India, Jul. 13–14, 2018.

[9] Guessasma, S. and S. Belhabib, "Infill strategy in 3D printed PLA carbon composites: Effect on tensile performance," *Polymers*, Vol. 14, No. 19, 4221, Oct. 2022.

[10] Sabouroux, P. and D. Ba, "Epsimu, a tool for dielectric properties measurement of porous media: Application in wet granular materials characterization," *Progress In Electromagnetics Research B*, Vol. 29, 191–207, 2011.

[11] Scotti, C., S. Enoch, M. Groisil, and N. Mallejac, "Characterization of inhomogeneous FDM manufactured materials: Comparison of free-space and mixing laws," *Progress In Electromagnetics Research M*, Vol. 134, 59–67, 2025.

[12] Poyanco, J.-M., F. Pizarro, and E. Rajo-Iglesias, "3D-printing for transformation optics in electromagnetic high-frequency lens applications," *Materials*, Vol. 13, No. 12, 2700, Jun. 2020.

[13] Kadhum, A. H., S. Al-Zubaidi, and S. S. Abdulkareem, "Effect of the infill patterns on the mechanical and surface characteristics of 3D printing of PLA, PLA+ and PETG materials," *Chemengineering*, Vol. 7, No. 3, 46, May 2023.

[14] Goulas, A., S. Zhang, J. R. McGhee, D. A. Cadman, W. G. Whittow, J. C. V. Yiannis, and D. S. Engstrøm, "Fused filament fabrication of functionally graded polymer composites with variable relative permittivity for microwave devices," *Materials & Design*, Vol. 193, 108871, Aug. 2020.

[15] Dahri, M. H., M. H. Jamaluddin, F. C. Seman, M. I. Abbasi, N. F. Sallehuddin, A. Y. I. Ashyap, and M. R. Kamarudin, "Aspects of efficiency enhancement in reflectarrays with analytical investigation and accurate measurement," *Electronics*, Vol. 9, No. 11, 1887, Nov. 2020.